RESEARCH ARTICLE

Droplet WILEY

Tuning static drop friction

Alexandre Laroche[1] | Abhinav Naga[1] | Chirag Hinduja[1] |
Azadeh Aghili Sharifi[1] | Alexander Saal[1] | Hyeonjin Kim[2] | Nan Gao[3] |
Sanghyuk Wooh[2] | Hans-Jürgen Butt[1] | Rüdiger Berger[1] | Doris Vollmer[1]

[1]Physics at Interfaces, Max Planck Institute for Polymer Research, Mainz, Germany

[2]School of Chemical Engineering & Materials Science, Chung-Ang University, Seoul, Republic of Korea

[3]Department of Mechanical Engineering, University of Birmingham, Birmingham, UK

Correspondence
Doris Vollmer, Physics at Interfaces, Max Planck Institute for Polymer Research, Ackermannweg 10, 55116 Mainz, Germany.
Email: vollmerd@mpip-mainz.mpg.de

Funding information
Deutsche Forschungsgemeinschaft, Grant/Award Numbers: Collaborative Research Centre 1194, Priority Programme 2171; The European Union's Horizon 2020 Research and Innovation Programme, Grant/Award Number: Advanced grant DynaMo, No. 883631; The Max Planck - University of Twente Center for Complex Fluid Dynamics

Abstract

The friction force opposing the onset of motion of a drop on a solid surface is typically considered to be a material property for a fixed drop volume on a given surface. However, here we show that even for a fixed drop volume, the static friction force can be tuned by over 30% by preshaping the drop. The static friction usually exceeds the kinetic friction that the drop experiences when moving in a steady state. Both forces converge when the drop is prestretched in the direction of motion or when the drop shows low contact angle hysteresis. In contrast to static friction, kinetic friction is independent of preshaping the drop, that is, the drop history. Kinetic friction forces reflect the material properties.

INTRODUCTION

From driving in the rain, it is known that some drops adhere to the windowpane of the car until a certain driving speed is exceeded. The minimum driving speed to set a drop in motion depends on the volume of the drop and the properties of the surface, such as its chemical composition and roughness.[1,2] In general, drops slide off a tilted surface if the gravitational force exceeds the static friction force.[3–6] However, the onset of motion can greatly vary on the same surface, raising the question: what controls the static friction, and how can we tune it?

The onset of motion is critical for many spray coating and printing processes. It determines the roll-off speed of drops in pool boiling heat transfer,[7] and the self-cleaning behavior of (super) liquid-repellent surfaces.[8,9] The onset of motion can be measured using external forces to move the drop, including gravitational, centrifugal,[10,11] magnetic,[12] or capillary forces.[13,14] Most commonly, the tilted plane method is used, where a drop is deposited on a surface that is to be slowly tilted by an angle α until the drop starts sliding.[15,16] The drop slides off the surface as soon as the gravitational force $F_G = \rho V g \sin\alpha$ overcomes the maximum static friction force, here termed, F_S, where ρ is the density of the liquid drop, V is its volume, and g is the gravitational acceleration. It has been shown that the static friction force of a drop on a solid surface can be equal to the maximum net horizontal component of the liquid–air surface

---

tension γ along the solid–liquid–air three-phase contact line opposite to the direction of motion:[5,6,14–18]

$$F_S = k \cdot w \cdot \gamma \cdot (\cos\theta_{Rear} - \cos\theta_{Front}). \quad (1)$$

Here, w is the drop contact width and θ_{Rear} and θ_{Front} are the apparent rear and front contact angles of the drop, respectively. The dimensionless factor k accounts for the shape of the contact line and angular variations of the contact angle around the contact line.[19] In the following, we used $k = 1$ for simplicity. Overcoming the static friction force is associated with a change in the shape of the drop.[3,15,16,19] When the drop is in continuous motion, kinetic friction opposes the motion. In this case, contact line friction is given by Equation (1) if k, w, and θ_{Rear} and θ_{Front} are replaced by their velocity-dependent values $k(v)$, $w(v)$, and $\theta_{Rear}(v)$ and $\theta_{Front}(v)$.

The static and the kinetic friction force between a drop and a surface have been measured using a dynamic adhesion force instrument (DAFI). Here, a cantilever is used as the force sensor, whereby a capillary, ring, or blade pushes or pulls a drop along a surface at a constant speed.[14,20–24] The deflection of the cantilever Δx multiplied by the spring constant of the capillary k_{spring} reveals the force needed to displace the drop $F_H = k_{spring}\Delta x$ (Hooke's law). This setup opens a new avenue to characterize drops on surfaces. It allows both the static and kinetic friction force to be monitored continuously, but more notably, the transition between the two states may be monitored.[20] Furthermore, DAFI extends the range of the external driving force, which is otherwise limited to the gravitational force in the case of the tilted-plane setups. Thus, static and kinetic friction can be quantified for drops that would otherwise remain stuck on tilted-plane setups even when the plane is positioned vertically. Typically, the force–displacement curves obtained with DAFI resemble those between two solid surfaces: a threshold force needs to be overcome before the two bodies slide over each other with a relatively lower steady force.[25] However, as opposed to solid–solid friction, in the liquid drop-solid case, the decrease in friction force between kinetic and static cases is brought upon by a change in the shape of the drop. Other differences have also been pointed out, such as time-dependent friction behavior and how both a decrease and an increase in normal force can increase apparent drop friction.[10,26]

Here, we demonstrate how the static friction force is strongly influenced by the drop history. The static friction force of a drop of a fixed volume can be tuned by preshaping the three-phase contact line.[27] Depending on the direction in which the drop is elongated with respect to the direction of motion, F_S can vary by more than 30% for drops with the identical volume on the same surface. This finding holds for surfaces with widely different wetting characteristics, for example, for drops that partially wet a surface to drops in the Cassie state on a superhydrophobic surface. Unlike static friction, the steady-state kinetic friction force does not depend on the drop history. The static and steady-state kinetic friction force converges when drops are pre-elongated along the direction of motion and when the contact angle hysteresis between the drop and the surface is low.

RESULTS

Most surfaces exhibit a water contact angle hysteresis >10° owing to surface roughness.[25,28] To mimic those surfaces, we use a micropillar array to gain insight into the reproducibility of the drops' sliding angle (Figure 1a,b). The array consists of cylindrical pillars having a diameter of 30 μm, a pillar–pillar spacing of 60 μm, and a height of 5 μm (Figure 1b). The pillars are coated with 1H-,1H-,2H-,2H-(perfluorodecyl) trichlorosilane to increase hydrophobicity. The large spacing and small pillar height ensure that a deposited drop wets the surface; that is, the drop is in the Wenzel state.[25,29] To measure the sliding angle α, the surface is tilted by 0.5°/s (KRÜSS, DSA100). We define the sliding angle as the angle where both the back and the
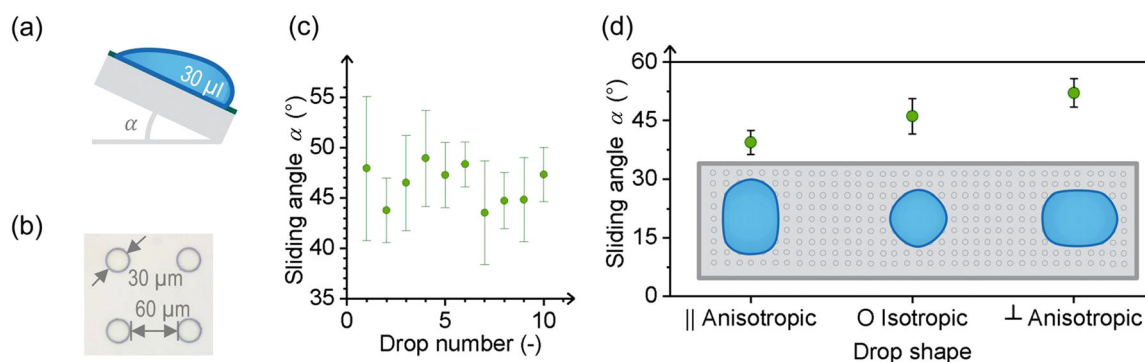
FIGURE 1   The ambiguity related to tilting plane experiments. (a) Illustration of tilting plane experiment. The sliding angle, α, of a drop of volume V (here 30 μl, $Bo = 0.13$) is defined as the tilt angle where the drop moves. (b) Optical microscope image of SU-8 pillars showing circular shape, diameter, and spacing. (c) Sliding angles measured on wetted fluorinated SU-8 pillars, showing the variation with consecutive measurements. Uncertainty bars represent ambiguity in the interpretation of the initiation of sliding. (d) Sliding angle results for anisotropic water drops on SU-8 pillars, where the major axis of the drop was parallel (‖) to the direction of subsequent motion after tilting, isotropic (O), or perpendicular (⊥).

front side of the drop are in motion. The sliding angle varies between 43° and 49° for successive repetitions, while the drop volume is fixed at 30 μl (Figure 1c, Supporting Information: Video 1). For these drop volumes, the Bond number is $Bo = \rho g R^2 / \gamma = 0.133$, where ρ is the density, g is the gravitational acceleration, and R is the drop radius. Moreover, for all drops investigated in the following, inertial effects can be neglected because the nominal Reynolds number $Re \sim \rho L v / \mu$ varies between $10^{-6} < Re < 10^{-3}$, where v is the velocity, and L is the length of the drop. To test the dependence of α on the initial drop shape, we investigated three different initial drop shapes (left to right, inset Figure 1d): an anisotropic drop with its major axis in line with the direction of gravitational force (parallel, "∥ anisotropic"), a drop shaped like a spherical cap ("O isotropic"), and an anisotropic drop with its major axis perpendicular to gravitational force (perpendicular, "⊥ anisotropic"). Indeed, the parallel drop started moving at a tilt angle of 37° (Supporting Information: Video 2), while that tilt angle had to be increased by a further 13° (to 52°) to

move the perpendicular drop (Supporting Information: Video 3). Thus, the sliding angle strongly depends on drop history.

To test how well the static friction force measured with the DAFI agrees with the force measured using a tilted plane setup, we measured both for a range of drop volumes in the symmetric drop case. A minimum drop volume of 20 μl was needed such that the gravitational force overcomes the static friction force. Smaller drops remained stuck to the surface. The corresponding static friction forces measured by DAFI are shown as blue circles in Figure 2a. The measured forces agree with the forces calculated using Equation (1). Here, we inserted the initial contact length as the width and contact angle, $\theta_{Rear} = 81°$ and $\theta_{Front} = 128°$. It ought to be noted, the contact width can slightly decrease before passing the threshold force, while the difference between the rear and front contact angles increases.[20] The agreement between experimental and calculated forces suggests that these contributions counter each other. The static friction force measured by DAFI is in good agreement with the forces measured
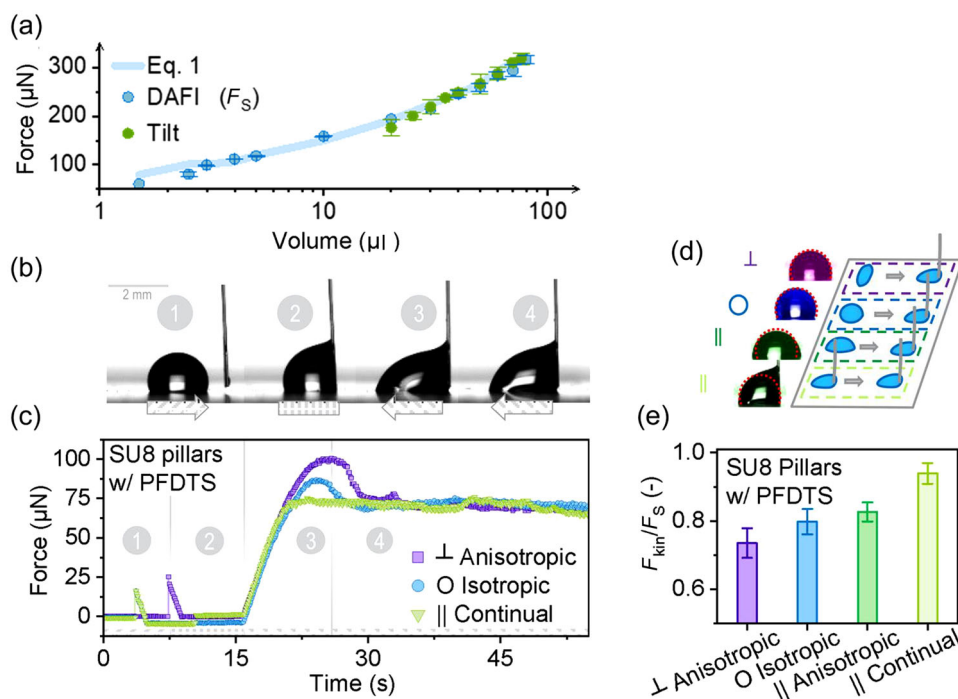

FIGURE 2 Force measurements on wetted fluorinated SU-8 pillars. (a) Drop adhesion force on fluorinated SU-8 pillars measured by DAFI (blue circles) and by tilting plane (green circles) for an isotropic drop with volumes between 1.5 and 80 μl ($0.02 < Bo < 0.25$, $10^{-6} < Re < 10^{-3}$). Calculated forces are shown as a transparent blue line (Equation 1). The deviations for drop volumes <3 μl are likely due to a larger relative influence of the capillary. The attraction between the drop and the capillary can result in a minor reduction of the contact width, resulting in a slightly lower measured F_S. (b) A side-view of a 3 μl water drop being pulled on a surface, with (1) its initial shape and undeformed force sensor, (2) after the force sensor "snapped-in" to the droplet, (3) pulling of the drop causing the onset of motion (most deformed state) and (4) steady dragging of the drop, $v = 0.2$ mm/s. Hashed arrows point in the direction of motion of the stage during each phase (forward hash indicates motion to the right, vertical hash is no motion, and backward hash indicates motion to the left). After relaxation for 10 s, the direction of motion was reversed. (c) Measured force curves plotted with time for a 3 μl drop in the perpendicular anisotropic (purple squares), isotropic (blue circles), and parallel continual (downward green triangles) measurement protocols. Hashed bars indicate the direction of motion of the stage, corresponding to (a). (d) Four measurement protocols based on different initial drop shapes, perpendicular anisotropic, isotropic, parallel anisotropic, and parallel without removing the capillary (parallel continual). Falsely colored drop images are representative of each protocol. An overlayed, dashed, red outline shows the shape of the symmetric drop condition for comparison. (e) A summary of the force curves represented as kinetic-to-threshold (or "static friction") friction force ratio for the four measurement protocols. DAFI, dynamic adhesion force instrument; PFDTS, 1H-,1H-,2H-,2H-perfluorodecyltrichlorosilane.

using the tilted-plane setup. DAFI, however, has two major advantages: (1) it extends the measurement range to smaller drop volumes, and (2) it allows us to measure the transition from the onset of motion to steady-state motion.

To quantify the temporal development of the forces, a drop is pulled in a direction either along its major axis or perpendicular to it (Figure 2b and Suporting Information: Video 4). Four scenarios of drop shaping are seen during such an experiment, where the micropillar array with the drop is moved at a constant velocity of $v = 0.2$mm/s (Figure 2c and Supporting Information: Videos 4–7). The horizontal position of the capillary apex marks the null-force state (image [1], Figure 2b). As the capillary approaches the drop, capillary forces generate an attractive force, which causes a sudden "snap-in" (regime [2], Figure 2c, time 4 and 7 s). Here, positive corresponds to a deflection of the capillary to the left of its equilibrium position. As the stage continues to move, the apparent force from the capillary decreases until stage motion stops (image [2], Figure 2b). The system is left undisturbed for 10 s for it to relax. We found that there is better reproducibility when the capillary pulls the drop instead of pushing it. Therefore, after the drop-capillary system relaxes, we change the direction of motion. Thus, for the measurement of the static and kinetic friction force, the stage is moved continuously in the opposite direction of the capillary, that is, toward the left in Figure 2b. Again, the force

measured by the capillary is positive, reflecting the resistive force needed to set the drop in motion and the friction force. The force steadily increases (regime [3], Figure 2b,c). The drop deforms into an elongated shape (image [3], Figure 2b). The slope of the force curve is independent of the initial drop shape but dependent on the spring constant of the capillary (Supporting Information: Figure S1). After the left-most three-phase-contact-point de-pins from the surface, the force peaks (Supporting Information: Figure S3). The presence and magnitude of the maximum depend on the preshaping of the drop.

After passing F_S, the drop takes its steady kinetic shape (regime [4] in Figure 2b,c). The drop keeps its shape for the parallel continual protocol. Independent of the protocol, the friction force F_{kin} remains constant. The small variations in force reflect the homogeneity of the surface, that is, small pinning sites.[30–32] The static friction force approaches the kinetic friction force for a drop pre-elongated in the direction of motion ("parallel continual" protocol). The ratio between F_{kin} and F_S varies from approximately 0.75 for perpendicularly elongated drops to close to 1 for the "parallel continual" protocol (Figure 2e). Thus, the ratio between F_{kin} and F_S reflects the difference between the initial drop shape and the shape under continuous motion.

To confirm that the static friction depends on the drop history while the steady-state kinetic friction is independent of the history, we investigate three additional surfaces (Figure 3a): a smooth
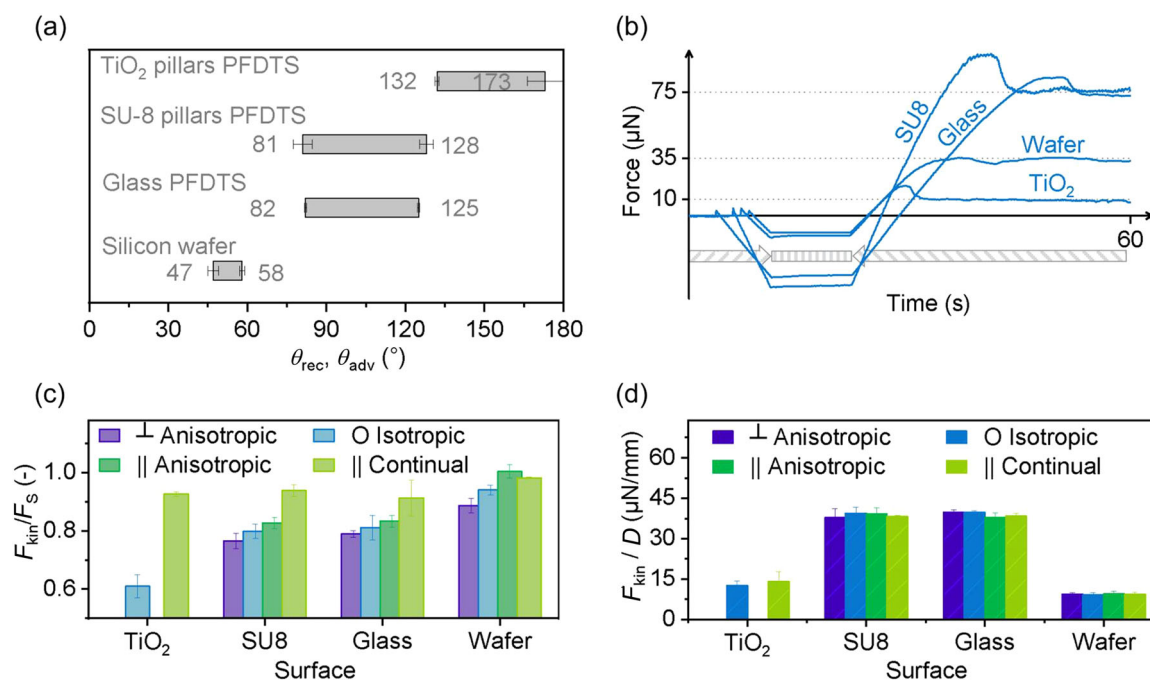

FIGURE 3 Results of force measurements on pillared (SU-8 and TiO$_2$) and flat (wafer and glass) surfaces coated with PFDTS (except for wafer). (a) Advancing and receding contact angles of water on each of the surfaces. Contact angle hysteresis is sketched by the gray box. (b) Exemplary force curves of 3 µl water on fluorinated titanium dioxide micro-pillars, fluorinated SU-8 pillars, fluorinated glass, and a hydrophilic silicon wafer. (c) Kinetic-to-threshold force ratio for different initial drop shapes, perpendicular anisotropic (purple), isotropic (blue), parallel anisotropic (dark green), and parallel continual (light green); and on four different surfaces, fluorinated titanium dioxide micropillars (TiO$_2$), fluorinated SU-8 micropillars (SU8), fluorinated glass (glass), and a silicon wafer (wafer). (d) Kinetic force to initial drop contact diameter ratio for the same four test conditions, and four surfaces. Drop speed 0.2 mm/s, drop volume 3 µl (except TiO$_2$ [8 µl], and anisotropic wafer [50 µl]). PFDTS, 1H-,1H-,2H-,2H-perfluorodecyltrichlorosilane.

hydrophilic silicon wafer, a smooth fluorinated glass slide (hydrophobic), and a superhydrophobic surface formed by fluorinated titania micropillars;[33] for details of their preparation see the Methods section. We follow the same protocol as depicted in Figure 2b. Pushing a symmetric drop over each of these surfaces yields a negative resistive force as the capillary presses up against the drop, resulting in a deflection to the right (Figure 3b). Motion is stopped and the system is left to relax for 10 s (constant force). Then the direction of motion changes, accompanied by a change in the sign of the force. The force increases as the drop begin to be pulled and deformed. The force peaks at a threshold, after which it descends to a stable kinetic force regime. Despite the similar shape of the force curves, the absolute values differ. For the same drop volume (3 µl) the static friction force was 12 µN on the superhydrophobic titania micropillars, while it exceeded 70 µN on the fluorinated glass slide and fluorinated SU-8 micropillars (Figure 3b).

According to Equation (1), the static friction force depends on the contact angles and the contact width of the drop with the substrate. The hydrophilic silicon wafer had the lowest contact angles, but also a low contact angle hysteresis $\Delta\theta = 11°$ (Figure 3a). Despite the low contact angle hysteresis, the comparatively large drop contact width (2.8 mm compared to 1.8 mm on SU-8 micropillars) results in a threshold force of $F_S = 36$ µN. The superhydrophobic titania micropillars show the lowest absolute force values caused by the low contact width (0.9 mm), outweighing the large contact angle hysteresis $\Delta\theta \approx 41°$.[34] The hydrophobic micropillars and the fluorinated glass surface have similar advancing and receding contact angles and contact widths. Correspondingly, the forces are comparable. The ratio between the kinetic and threshold force can be tuned by more than 30% by changing the drop shape (Figure 3c). The hydrophilic silicon wafer shows the smallest dependence of the ratio between F_{kin} and F_S on the initial drop shape, while the superhydrophobic titania micropillars show the largest dependence. The high mobility of drops on superhydrophobic surfaces renders visible elongation of the drop impossible. Therefore, the data are missing. The ratio between F_{kin} and F_S exceeds 0.9 on all surfaces when the motion is continued without removing the capillary from the drop ("parallel continual"). Resumption of motion requires little reshaping of the drop. In contrast to the pronounced dependence of F_S and the ratio between F_{kin} and F_S on the drop shape, the kinetic force does not depend on the initial drop shape (Figure 3d). This holds for all surfaces, independent of their hydrophilicity and roughness.

DISCUSSION

The kinetic friction force measured at low speed ($Ca < 10^{-5}$) is attributed to contact line friction. Since $Ca \ll 1$, viscous dissipation in the bulk of the drop is small compared to contact line friction.[26] The difference between the static and kinetic friction force reflects the different shapes of the three-phase contact line, in particular the advancing and receding contact angle as well as the contact width.[20] This difference is eliminated when the initial shape of the stationary three-phase contact line is tuned to its dynamic state.

According to measurements performed by Gao et al.[20] the kinetic and static friction force hardly depend on Ca for $Ca < 10^{-5}$. In general drop velocity, interfacial tension and viscous dissipation play a role in determining the kinetic friction force for different surfaces.[35] Here, we focus our experiments on being able to influence the static friction force. We keep the kinetic friction force, and therefore viscous dissipation, constant for a given surface throughout the experiments by using a single liquid, water, and a constant speed of 0.2 mm/s. This constant speed is in contrast with tilting plate experiments, where the speed of the drop typically increases until the kinetic friction finally becomes great enough to balance the gravitational force.

If one considers the hydrophobic pillared surfaces such as SU-8 micropillars and the titanium dioxide (TiO_2) micropillars, the static friction force follows the energy needed to break the capillary bridges over the pillars.[36] If the force per pillar detachment is constant, then it is proportional to the number of pillars being detached at any one time. For the droplet-surface combinations tested, as the trailing end of the drop (detaching end) approaches the widest portion of the drop (or when the trailing edge becomes the widest), the force increases to a maximum (Supporting Information: Figure S3). Once that maximum has been overcome, there is an excess force for detaching the remaining pillars at a smaller width, resulting in a rapid reshaping of the macroscopic contact line, and a reduction in force. The steady kinetic friction force, therefore, reflects a balance between the force applied and the detachment of further pillars, where the width of the drop is relatively constant along its length—although the width remains to be experimentally measured, its 3D shape can be qualitatively visualized (Supporting Information: Video 8 and Figure S3f).

CONCLUSION

Preshaping the three-phase contact line of a drop on a solid surface can be used as a means to minimize the maximum static friction force, relevant in applications where the easy shedding of liquids is required. Preshaping could, for example, be induced by chemically or topographically structuring a surface to favor drop elongations parallel to the direction of motion.[37–39] For condensation drop shedding, it means with careful surface patterning, one can induce drop shedding sooner by aligning drops with the gravitational vector.[40] Elongated drops also have the attribute of larger surface area compared to spherical or symmetric droplets, and such can be advantageous for heat transfer and evaporation applications.[41]

With the DAFI used in this work, the static and the kinetic friction force can be measured for a large range of drop sizes and velocities without information on the three-phase contact line, that is, on the advancing and receding contact angle, the contact width and the k-factor. On the other hand, if these parameters are given, dynamic adhesion force measurements can be used to distinguish

between contributions of contact line friction and further contributions. These might result from Stokes friction, a ridge formation, and shear thinning or thickening for non-Newtonian liquids.

METHODS

Four surfaces were used, including a smooth silicon wafer, SU-8 pillars on glass, smooth glass, and TiO_2 micropillars. All surfaces were fluorinated except the silicon wafer.

A 1-mm-thick round silicon wafer (150 mm diameter) was split in half. One half-moon-shaped piece was used for water drop friction tests.

The rigid micropillar surface was manufactured by spin-coating an epoxy-based SU-8 photoresist (SU-8 5; MicroChem) on a glass slide (24×60 mm^2, 170 ± 5 μm thickness; Menzel-Glaser). The glass slides were cleaned with acetone and subsequently activated by oxygen plasma under 300 W for 5 min. The SU-8 photoresist was then spin-coated (500 rpm for 5 s followed by 3000 rpm for 30 s; SÜSS MicroTec) on the glass slides. The coated slides were heated at 65°C for 3 min, 95°C for 10 min, and then at 65°C for 30 min, respectively. Subsequently, the samples were slowly cooled down within 2 h and exposed to UV light (mercury lamp; 350 W) under a photolithography mask for 14 s (masker aligner SÜSS MicroTec MJB3 UV400). To cross-link the photoresist, the samples were heated at 65°C for 1 min, 95°C for 3 min, and 65°C for 30 min and then cooled down slowly. Next, the samples were immersed in the SU-8 developer solution for 6 min, washed with isopropanol and deionized water, and then dried in air.

TiO_2 cylindrical micropillar arrays were prepared at Chung-Ang University in South Korea. For mold materials, polyurethane acrylate (PUA, MINS 301 RM; Minuta Tech) and polydimethylsiloxane (PDMS, Sylgard 184 Silicon Elastomer; Dow Corning) were used. TiO_2 pastes (DSL 18 NR-D; Dyesol) were used to fabricate multiscale hierarchical TiO_2 surfaces.

UV-assisted micromolding of pillar patterns: A silicon master pattern (with 10 μm in diameter and 10 μm in height), fabricated by photolithography, was used as a basis mold to prepare PUA replica patterns by replica molding with homogeneous mixtures of acrylate-functionalized polysiloxane and multifunctional acrylated prepolymer (PUA, MINS 301 RM). An intensely stirred mixture of PDMS precursors and crosslinkers (10:1 by weight) with air bubbles was poured onto the PUA master and evacuated in a vacuum desiccator for more than 30 min until all the air bubbles were removed. The PDMS precursors were placed in a convection oven at 60°C for 6 h to achieve fully heat-cured PDMS.

To create the TiO_2 micropillars (Figure 4), TiO_2 paste was doctor bladed onto a silicon wafer substrate. The PDMS micropillar pattern was imprinted onto the layer of TiO_2 paste, and was placed in an oven at 60°C to solidify the paste. After removal of the PDMS mold, the TiO_2 pillars on silicon were placed in a furnace at 500°C for 30 min to remove residual organics.

To make the pillars hydrophobic, a vapor-phase deposition of 1H-,1H-,2H-,2H-perfluorodecyltrichlorosilane (PFDTS; Alfa-Aesar) was performed. The substrates were first activated in an oxygen plasma for 2 min at reduced power. They were then placed in a sealed reaction chamber with the PFDTS and a vacuum was drawn. After 2 h, the substrates were withdrawn from the chamber and placed in a vacuum oven (room temperature) for 10 min.

Contact angle, sliding angle, and friction force measurements were carried out using a Krüss DSA-100 goniometer (Krüss). The device was equipped with a motorized syringe holder, drop dispenser, tilt axis, and x- and y-stage. For the force measurements, a custom-built holder was fabricated to fit into the syringe grips of the goniometer and to accommodate a glass capillary cantilever force sensor. The sensor was calibrated at 300 μN/mm (see force sensor calibration). For force measurements, the stage speed was 0.20 mm/s. The tilt axis speed for sliding angle measurements was 1°/min.

A 20 μl water drop was deposited on the surface using the software-controlled dosing unit and a 100 μl syringe (No. 1710) equipped with a 0.29 mm needle. After dosing was completed, the syringe was lifted using the software-controlled syringe lifter and the stage was tilted at a rate of 0.5°/min. Contact angle and drop position measurements were collected at a rate of 1 fps. The roll-off angle was identified using the left three-phase-contact point and the right three-phase contact point determined by the Krüss Advance software. The contact point with frame number data was exported from Advance into Microsoft Excel. The displacement of each contact point with respect to the tilt angle was determined. The roll-off angle was selected as the tilt angle at which both the left and right contact points had moved by at least 0.3 mm from their original position. The resolution of the software-generated data was to the nearest 0.1 mm. To measure dependence on drop size, the same protocol
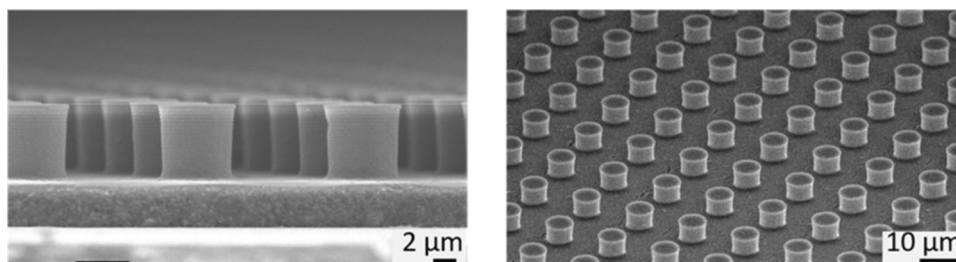

FIGURE 4 TiO_2 pillars on a silicon substrate. Pillar edge-to-edge spacing of 7.5 μm, diameter 7 μm, and height 9 μm. TiO_2, titanium dioxide.
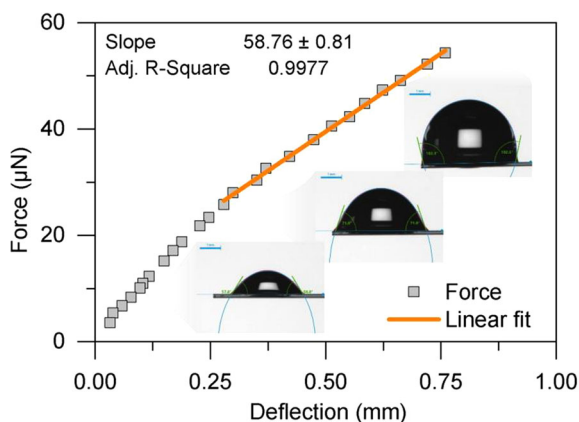
FIGURE 5 Spring constant calibration curve for a glass capillary cantilever with spring constant 59 µN/mm using the quasi-static gravitational-deflection method. Inset images show the shape of the water drop at specific data points. Volume calculations of the drop that caused a deflection less than 0.25 mm were likely inaccurate due to an elongated drop shape and were therefore not included in the linear regression analysis.

was repeated with different drops for at least three repetitions. After each sliding drop, the sample was repositioned using software-controlled x-/y-axes.

A sample was laid on the Krüss DSA-100 goniometer stage. A solid brass cylinder was installed instead of a syringe on the motorized syringe holder. A brass stub in which was fixed a glass capillary (described in "Sensor Calibration") was screwed into the solid brass cylinder such that the capillary hung down above the sample. The motorized syringe holder was lowered until the glass capillary nearly made contact with the surface. A water drop of controlled volume (typically 3 µl) was deposited in contact with the sample surface and the glass capillary using a mechanical pipette (Eppendorf). An automated sequence was then initiated: the capillary was raised such that the drop sat only on the sample surface. The stage moved backward by 5 mm to create a space between the drop and the capillary. Then the capillary was lowered, and the stage was slowly moved forward until the capillary "snapped-into" contact with the drop. After 5 s of resting time, the stage was moved backward at a constant speed of 0.20 mm/s for a distance of 8 mm such that the capillary was pulling the drop over the surface. During this sequence, a video was recorded through the Krüss Advance software. The capillary deflection was later extracted from the video using image analysis.

For prestretching of drops, the procedure was followed as described above until the snap-in of the capillary with the drop. At that point, the stage was moved forward at 50 mm/s such that the drop would be pulled but the capillary would escape.

Cantilever force sensors were fabricated from hollow rectangular borosilicate glass capillaries, with an inner hole size 0.50 × 5.00 and 50 mm long (CM Scientific). They were adhered (2-K-epoxyglue; UHU) into cylindrical brass holders by a 5.00 mm-deep hole, resulting in a 45 mm cantilever. Two methods of force calibration were performed, dynamic, and quasi-static. In the dynamic method, the cantilever was given an initial displacement, then released. Its displacement at its

natural mode of vibration was recorded using the camera on the goniometer set to record at 1000 fps. The period of vibration was then used to compute the natural frequency, then the relation was used $k_{dyn} = 0.243 m\omega_n^2$, where k_{dyn} was the dynamic spring constant, m was the mass of the glass capillary cantilever (45 mm length), and ω_n was the natural frequency of the cantilever. The quasi-static method involved tracking the maximum displacement of the cantilever under an applied load. The load used was the weight of a drop of known volume. A 3 µl water drop was deposited on the tip of the cantilever, and the cantilever deflection was recorded with time. As time passed, the drop evaporated, thereby gradually decreasing the applied load (Figure 5). The slope of the load-displacement curve yielded k_{stat}, the static spring constant. The time-dependent drop volume was calculated by an image-fitting algorithm in the Krüss Advance software. Due to the changing shape of the drop as a function of volume, the volume calculation algorithm likely had reduced accuracy. Therefore, the linear regression to determine the slope, and therefore the spring constant, only included larger drop volumes.

CONFLICT OF INTEREST

The authors declare no conflict of interest.

ORCID

Alexandre Laroche http://orcid.org/0000-0002-7041-7181
Abhinav Naga http://orcid.org/0000-0001-7158-622X
Nan Gao http://orcid.org/0000-0001-7510-2886
Sanghyuk Wooh https://orcid.org/0000-0002-6535-370X
Hans-Jürgen Butt http://orcid.org/0000-0001-5391-2618
Rüdiger Berger https://orcid.org/0000-0002-4084-0675
Doris Vollmer https://orcid.org/0000-0001-9599-5589

REFERENCES

1. Extrand CW, Kumagai Y. Liquid drops on an inclined plane: the relation between contact angles, drop shape, and retentive force. *J Colloid Interface Sci*. 1995;170:515-521.
2. Tadmor R. Open problems in wetting phenomena: pinning retention forces. *Langmuir*. 2021;37:6357-6372.
3. Semprebon C, Brinkmann M. On the onset of motion of sliding drops. *Soft Matter*. 2014;10:3325-3334.
4. Krasovitski B, Marmur A. Drops down the hill: theoretical study of limiting contact angles and the hysteresis range on a tilted plate. *Langmuir*. 2005;21:3881-3885.
5. Pierce E, Carmona FJ, Amirfazli A. Understanding of sliding and contact angle results in tilted plate experiments. *Colloids Surf A*. 2008;323:73-82.

6. ElSherbini AI, Jacobi AM. Retention forces and contact angles for critical liquid drops on non-horizontal surfaces. *J Colloid Interface Sci.* 2006;299:841-849.

7. Chu KH, Enright R, Wang EN. Structured surfaces for enhanced pool boiling heat transfer. *Appl Phys Lett.* 2012;100:241603.

8. Tuteja A, Choi W, Mabry JM, McKinley GH, Cohen RE. Designing super-oleophobic surfaces with fluoroposs. *2007 AIChE Annu Meet.* 2007;1618-1623.

9. Deng X, Mammen L, Butt H-J, Vollmer D. Candle soot as a template for a transparent robust superamphiphobic coating. *Science.* 2012;335:67-70.

10. Tadmor R, Bahadur P, Leh A, N'Guessan HE, Jaini R, Dang L. Measurement of lateral adhesion forces at the interface between a liquid drop and a substrate. *Phys Rev Lett.* 2009;103:266101.

11. Goodwin R, Rice D, Middleman S. A model for the onset of motion of a sessile liquid drop on a rotating disk. *J Colloid Interface Sci.* 1988;125:162-169.

12. Timonen JVI, Latikka M, Ikkala O, Ras RHA. Free-decay and resonant methods for investigating the fundamental limit of superhydrophobicity. *Nat Commun.* 2013;4:2398.

13. Mannetje D, Banpurkar A, Koppelman H, Duits MHG, Van Den Ende D, Mugele F. Electrically tunable wetting defects characterized by a simple capillary force sensor. *Langmuir.* 2013;29:9944-9949.

14. Pilat DW, Papadopoulos P, Schäffel D, Vollmer D, Berger R, Butt H-J. Dynamic measurement of the force required to move a liquid drop on a solid surface. *Langmuir.* 2012;28:16812-16820.

15. Bikerman JJ. Sliding of drops from surfaces of different roughnesses. *J Colloid Sci.* 1950;5:349-359.

16. Dussan V. EB, Chow RT-P. On the ability of drops or bubbles to stick to non-horizontal surfaces of solids. *J Fluid Mech.* 1983;137:1-29.

17. Kawasaki K. Study of wettability of polymers by sliding of water drop. *J Colloid Sci.* 1960;15:402-407.

18. Furmidge CGL. Studies at phase interfaces. I. The sliding of liquid drops on solid surfaces and a theory for spray retention. *J Colloid Sci.* 1962;17:309-324.

19. Extrand CW, Gent AN. Retention of liquid drops by solid surfaces. *J Colloid Interface Sci.* 1990;138:431-442.

20. Gao N, Geyer F, Pilat DW, et al. How drops start sliding over solid surfaces. *Nat Phys.* 2018;14:191-196.

21. Daniel D, Timonen JVI, Li R, Velling SJ, Aizenberg J. Oleoplaning droplets on lubricated surfaces. *Nat Phys.* 2017;13:1020-1025.

22. Hokkanen MJ, Backholm M, Vuckovac M, Zhou Q, Ras RHA. Force-based wetting characterization of stochastic superhydrophobic coatings at nanonewton sensitivity. *Adv Mater.* 2021;33:2105130.

23. Naga A, Kaltbeitzel A, Wong WSY, Hauer L, Butt HJ, Vollmer D. How a water drop removes a particle from a hydrophobic surface. *Soft Matter.* 2021;17:1746-1755.

24. Beitollahpoor M, Farzam M, Pesika NS. Determination of the sliding angle of water drops on surfaces from friction force measurements. *Langmuir.* 2022;38:2132-2136.

25. Nosonovsky M. Model for solid-liquid and solid-solid friction of rough surfaces with adhesion hysteresis. *J Chem Phys.* 2007;126:224701.

26. Bormashenko E, Bormashenko Y, Oleg G. On the nature of the friction between nonstick droplets and solid substrates. *Langmuir.* 2010;26:12479-12482.

27. Musterd M, Van Steijn V, Kleijn CR, Kreutzer MT. Droplets on inclined plates: local and global hysteresis of pinned capillary surfaces. *Phys Rev Lett.* 2014;113:066104.

28. Jung YC, Bhushan B. Contact angle, adhesion and friction properties of micro-and nanopatterned polymers for superhydrophobicity. *Nanotechnology.* 2006;17:4970-4980.

29. Wenzel RN. Resistance of solid surfaces to wetting by water. *Ind Eng Chem.* 1936;28:988-994.

30. Ling H, Srinivasan S, Golovin K, McKinley GH, Tuteja A, Katz J. High-resolution velocity measurement in the inner part of turbulent boundary layers over super-hydrophobic surfaces. *J Fluid Mech.* 2016;801:670-703.

31. Courbin L, Denieul E, Dressaire E, Roper M, Ajdari A, Stone HA. Imbibition by polygonal spreading on microdecorated surfaces. *Nat Mater.* 2007;6:661-664.

32. Kalinin YV, Berejnov V, Thorne RE. Contact line pinning by microfabricated patterns: effects of microscale topography. *Langmuir.* 2009;25:5391-5397.

33. Wooh S, Koh JH, Lee S, Yoon H, Char K. Trilevel-structured superhydrophobic pillar arrays with tunable optical functions. *Adv Funct Mater.* 2014;24:5550-5556.

34. Schellenberger F, Encinas N, Vollmer D, Butt H-J. How water advances on superhydrophobic surfaces. *Phys Rev Lett.* 2016;116:096101.

35. Mahadevan L, Pomeau Y. Rolling droplets. *Phys Fluids.* 1999;11:2449-2453.

36. Butt H-J, Gao N, Papadopoulos P, Steffen W, Kappl M, Berger R. Energy dissipation of moving drops on superhydrophobic and superoleophobic surfaces. *Langmuir.* 2016;33:107-116.

37. Raj R, Adera S, Enright R, Wang EN. High-resolution liquid patterns via three-dimensional droplet shape control. *Nat Commun.* 2014;5:4975.

38. Yoshimitsu Z, Nakajima A, Watanabe T, Hashimoto K. Effects of surface structure on the hydrophobicity and sliding behavior of water droplets. *Langmuir.* 2002;18:5818-5822.

39. Chen Y, He B, Lee J, Patankar NA. Anisotropy in the wetting of rough surfaces. *J Colloid Interface Sci.* 2005;281:458-464.

40. Li J, Zhou Y, Wang W, Du F, Ren L. A bio-inspired superhydrophobic surface for fog collection and directional water transport. *J Alloys Compd.* 2020;819:152968.

41. Nahar MM, Ma B, Guye K, et al. Review article: microscale evaporative cooling technologies for high heat flux microelectronics devices: background and recent advances. *Appl Therm Eng.* 2021;194:117109.

SUPPORTING INFORMATION

Additional supporting information can be found online in the Supporting Information section at the end of this article.